Kinetics Teach That Electronic Coupling Lowers the Free Energy Change that Accompanies Electron Transfer

Renato Sampaio[1], Eric Piechota[1], Ludovic Troian-Gautier[1], Andrew Maurer[2], Ke Hu[3], Phill Schauer[4], Amber Blair[4], Curtis Berlinguette[5], Gerald J. Meyer[6]

[1]University of North Carolina at Chapel Hill, [2]University of North Carolina at Chapel Hilll, [3]Fudan University, [4]The University of British Columbia, [5]University of British Columbia, [6]University of North Carolina

Submitted to Proceedings of the National Academy of Sciences of the United States of America

Electron transfer theories predict that an increase in the quantum mechanical mixing (H_{DA}) of electron donor and acceptor wavefunctions at the instant of electron transfer drives equilibrium constants toward unity. Kinetic and equilibrium studies of four acceptor-bridge-donor (A-B-D) compounds reported herein provide experimental validation of this prediction. The compounds have two redox active groups that differ only by the orientation of the aromatic bridge: a phenyl-thiophene bridge (p) that supports strong electronic coupling of H_{DA}> 1000 cm^{-1}; and a xylyl-thiophene bridge (x) that prevents planarization and decreases H_{DA}< 100 cm^{-1}without a significant change in distance. Pulsed light excitation allowed kinetic determination of the equilibrium constant, K_{eq}. In agreement with theory, $K_{eq}(p) < K_{eq}(x)$. A van't Hoff analysis provided clear evidence of an adiabatic electron transfer pathway for p and a non-adiabatic pathway for x. Collectively the data show that the absolute magnitude of the thermodynamic driving force for electron transfers in biology and chemistry are decreased when adiabatic pathways are operative,a finding that should be taken into account in the design of hybrid materials for solar energy conversion.

Electron Transfer | Electronic Coupling | Gibbs Free Energy | Equilibrium | Solar Energy

Introduction

Electron flow in natural photosynthesis is controlled, to a large extent, by the spatial arrangement of redox active species in the electron transport chain whose formal reduction potentials provide a free energy gradient.(1-6) In artificial photosynthesis, this same strategy has been employed to vectorially translate electrons away from interfaces or toward catalytic sites.(7-11). In each case, ideal electron flow occurs rapidly and quantitatively in one desired forward direction, without a significant loss in the Gibbs free energy, $^{\triangle}G^{o}$. In reality, electron transfer exists as an equilibrium with forward and reverse reactions regulated by the free energy that separates the redox active species, $|^{\triangle}G^{o}|$. When $|^{\triangle}G^{o}|$ approaches zero, the reverse reactions become more significant resulting in electron flow in undesired directions. Strong electronic coupling between redox centers facilitates rapid electron transfer, but theoretical considerations indicate that this will result in a free energy loss.(12, 13) Many scientists in the growing fields of artificial photosynthesis for electrical power generation or solar fuel production do not consider the influence of electronic coupling on $^{\triangle}G^{o}$. This may be due to the fact that the theory that relates electronic coupling and $^{\triangle}G^{o}$ has received little experimental attention.(14, 15)

Herein, we describe a new kinetic approach for quantifying the influence of electronic coupling on $^{\triangle}G^{o}$ that was applied to acceptor-bridge-donor compounds of the type shown in Fig. 1. The four cyclometalated ruthenium compounds shown contain an aromatic thiophene bridge to a triphenylamine (TPA) donor group. Electron withdrawing (-CF_3) or donating (-OMe, methoxy) substituents on the cyclometalating phenyl ring were used to tune the $Ru^{III/II}$ potentials while the identity of the $TPA^{+/0}$ was fixed. These compounds are ideal for fundamental study as they provide TPA → Ru^{III} electron transfer reactions that are thermodynamically unfavored (**1x**, **1p**), $^{\triangle}G^{o} > 0$, or favored (**2x**, **2p**), $^{\triangle}G^{o} < 0$. The influence of electronic coupling on the free energy change was elucidated by the introduction of groups that disrupt conjugation in the aromatic bridge. For compounds (**1p**, **2p**), a *phenyl* bridge unit allows planarity with the thiophene and thus promotes strong electronic coupling. On the contrary, the two methyl groups on the *xylyl* bridge of compounds (**1x**, **2x**) inhibit planarity with the thiophene and decrease electron coupling. The 14 Å geometric distance between the amine N and the Ru center, garnered from density functional theory (DFT) optimized structures, is the same for all four compounds such that the *through-space* electronic coupling is constant. The intense color changes associated with the $Ru^{III/II}$ and $TPA^{+/0}$ redox chemistry enables small concentrations to be detected spectroscopically. To our knowledge, the combined optical, redox, and structural properties of these compounds are the most optimal available in the literature for determination of how electronic coupling influences the free energy change of an electron transfer reaction.(16)

The theoretical prediction that electronic coupling, H_{DA}, lowers $^{\triangle}G^{o}$

Consider a simplified A-B-D compound in which the quantum mechanical interaction between an electron acceptor (A) and

Significance

Nature's use of electronic coupling (H_{DA}) and free energy (ΔG^{o}) gradients to vectorially control electron transport provides inspiration for artificial photosynthesis. Theoretical predictions indicate that H_{DA} and ΔG^{o} are not independent parameters, and are instead linked. Reported here is a new and broadly applicable kinetic approach that was utilized to demonstrate such behavior for four donor-bridge-acceptor compounds. When the electronic coupling was large and electron transfer was adiabatic, the free energy of the reaction, $|\Delta G^{o}|$, was less than that for non-adiabatic transfer. This finding should be taken into account in the design of hybrid materials for solar energy conversion and has broad implications to the many classes of electron transfer reactions in biology and chemistry.

Reserved for Publication Footnotes

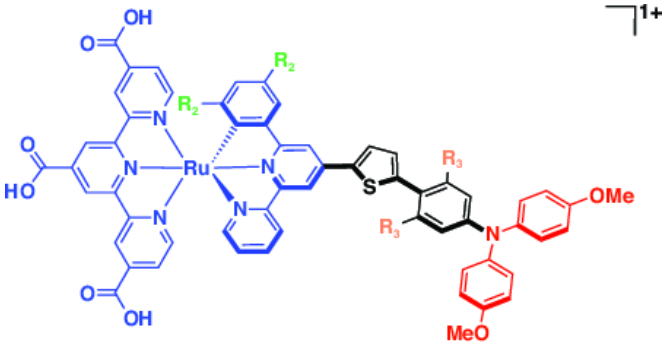

Fig. 1. The Acceptor-Bridge-Donor compounds utilized herein. Four cyclometalated ruthenium compounds with carboxylic acid groups (for binding to TiO_2) and an aromatic bridge to a triphenylamine (TPA). Methyl substituents in the R_3 positions of the *xylyl*-bridge (**x**) lowers electronic coupling relative to the *phenyl*-bridge (**p**). The R_1 and R_2 substituents allow the $E^o(Ru^{III/II})$ potentials be controlled for the 1 and 2 series while the $E^o(TPA^{+/0})$ was held at parity.

an electron donor (D) wavefunctions is controlled by the bridge (B) that links them. The degree of mixing is quantified by the electronic coupling matrix element H_{DA}. Marcus theory holds that the many-fold potential surfaces for electron-transfer can be represented as parabolic Gibbs free energy surfaces (GESs) with fixed force constants, for the A-B-D 'reactants' and the A^--B-D^+ 'products', that are a function of a single reaction coordinate, equation (1) and Fig. 2.(12, 13, 17) Robin and Day have categorized the degree of electronic coupling between A and D in three distinct classes, Fig. 2a.(18) When the bridge is insulating and no coupling occurs during the electron transfer, D and A retain their original identities and electron transfer occurs by a jump from the reactant to the product GES (Class I or nonadiabatic). At the opposite extreme where the bridge facilitates strong electronic coupling, the D and A GESs collapse to a single minimum GES (adiabatic Class III). Most common electron transfer reactions in biology and chemistry, however, occurs with intermediate electronic coupling in the double minimum GES (adiabatic Class II). Note that as H_{DA} increases in the progression from non-adiabatic to adiabatic Class II electron transfer, $|\Delta G^o|$ decreases to an adiabatic value, ΔG^o_{ad}, i.e. $|\Delta G^o| > |\Delta G^o_{ad}|$. This would indicate that the equilibrium and thus the directionality of electron transfer can be controlled by the nature of the bridge and its ability to promote electronic coupling. It is therefore of interest to test this prediction experimentally under a variety of conditions that include both weak and strong(14, 15) coupling.

The kinetic approach

The approach reported here exploits the *dynamic* aspect of equilibrium reactions through a broadly applicable kinetic model. Although equilibrium, as a 'balance of opposing forces', oftentimes invokes the false perception that the competing forces stop altogether as solution concentrations become time invariant,(19) in fact, a *dynamic* equilibrium is emphasized in introductory science class rooms where the opposing forces are rate constants, equation (1), whose values can be quite large and depend only on the absolute temperature.(20)

$$\text{A-B-D} \underset{k_{-1}}{\overset{k_1}{\rightleftharpoons}} \text{A}^-\text{-B-D}^+ \quad (1)$$

Rate constants provide a direct measure of the equilibrium constant, K_{eq}, that may also be computed from the difference in the acceptor (A) and the donor (D) formal reduction potentials, $\Delta E^o = E^o(A^{0/-}) - E^o(D^{+/0})$ through Faraday's constant (F), equation (2).

$$K_{eq} = e^{\frac{F\Delta E^o}{RT}} = e^{\frac{-\Delta G^o}{RT}} = \frac{k_1}{k_{-1}} \quad (2)$$

While relations like those given in equation (2) can be found in most introductory science books, direct estimates of K_{eq} values through independent electrochemical measurements of ΔE^o are only strictly correct for nonadiabatic electron transfer. Strong electronic interactions of the donor and acceptor redox orbitals at the instant of electron transfer will result in adiabatic electron transfer that is expected to decrease $|\Delta G^o|$ as was described above.(12, 13, 17) Indeed, under such conditions ΔE^o is no longer an accurate indicator of the equilibrium or the true free energy change. An alternative approach is to use kinetic data, yet previous attempts to quantify dynamic equilibria with pulsed-laser or line-broadening techniques have met limited success and have not provided temperature dependent K_{eq} values.(14, 15, 21-23) Kubiak and coworkers have previously investigated the influence of H_{DA} on $\Delta G°$ through the use of vibrational spectroscopy on 'mixed-valence isomers' which has shown that $|\Delta G°|$ in strongly coupled systems was less than values expected for non-adiabatic electron transfer.(14, 15)

The kinetic strategy utilizes a pulsed laser to initiate electron transfer to a secondary acceptor whose recombination kinetics are sufficiently slow such that the approach to A-B-D ⇋ A^--B-D^+ equilibrium can be time resolved spectroscopically. In this study, A-B-D compounds of the general form Ru^{II}-B-TPA, were anchored to the surface of TiO_2 anatase nanocrystallites that serves as the secondary acceptor. Upon light absorption by the Ru^{II} constituent, a charge transfer excited-state injects an electron into TiO_2 to form $TiO_2(e^-)$|-Ru^{III}-B-TPA, where Ru^{III}-B-TPA represents the A-B-D state of interest. Following electron injection, the TPA donor may transfer an electron to the oxidized Ru^{III} acceptor to give Ru^{II}-B-TPA^+, which establishes the A^--B-D^+ state.(16) Of critical importance, for all four compounds studied in this work, the Ru^{III}-B-TPA is the initial and reference A-B-D state after excited-state electron injection, such that electron transfer from the TPA donor to the Ru^{III} acceptor is thermodynamically unfavored for (**1x**, **1p**), and favored for (**2x**, **2p**) (see Table 1).The millisecond lifetime of the injected $TiO_2(e^-)$ electron and the intense color changes associated with the $Ru^{III/II}$ and $TPA^{+/0}$ redox chemistry, enabled the Ru^{III}-B-TPA ⇋ Ru^{II}-B-TPA^+ *dynamic* equilibria to be measured spectroscopically and quantified through the proposed kinetic model. It is recognized that this light-initiated reaction technically yields a 'quasi-equilibrium' since true equilibrium is achieved only when the injected electrons recombine with the oxidized compound. Nevertheless, related photochemical strategies have been widely utilized in fluid solution to characterize excited-state "equilibrium" reactions, most notably for the determination of excited-state pK_a* values of photo-acids and photo-bases in aqueous solutions.(24-26) Consequently, this kinetic approach is expected to be of general utility for characterization of free energy changes that accompany electron transfer in chemistry and biology.

Results and Discussions

The A-B-D compounds

All four compounds were available from our previous studies and their measured redox properties are summarized in Table 1.(16) Of note is the fact that the $E^o(TPA^{+/0})$ = 0.94 V *vs.* NHE for all four compounds and $E^o(Ru^{III/II})$ was 1.03 V for **2p**, 1.01 V for **2x**, and 0.86 V for **1x** and **1p**. For **2p** in particular,

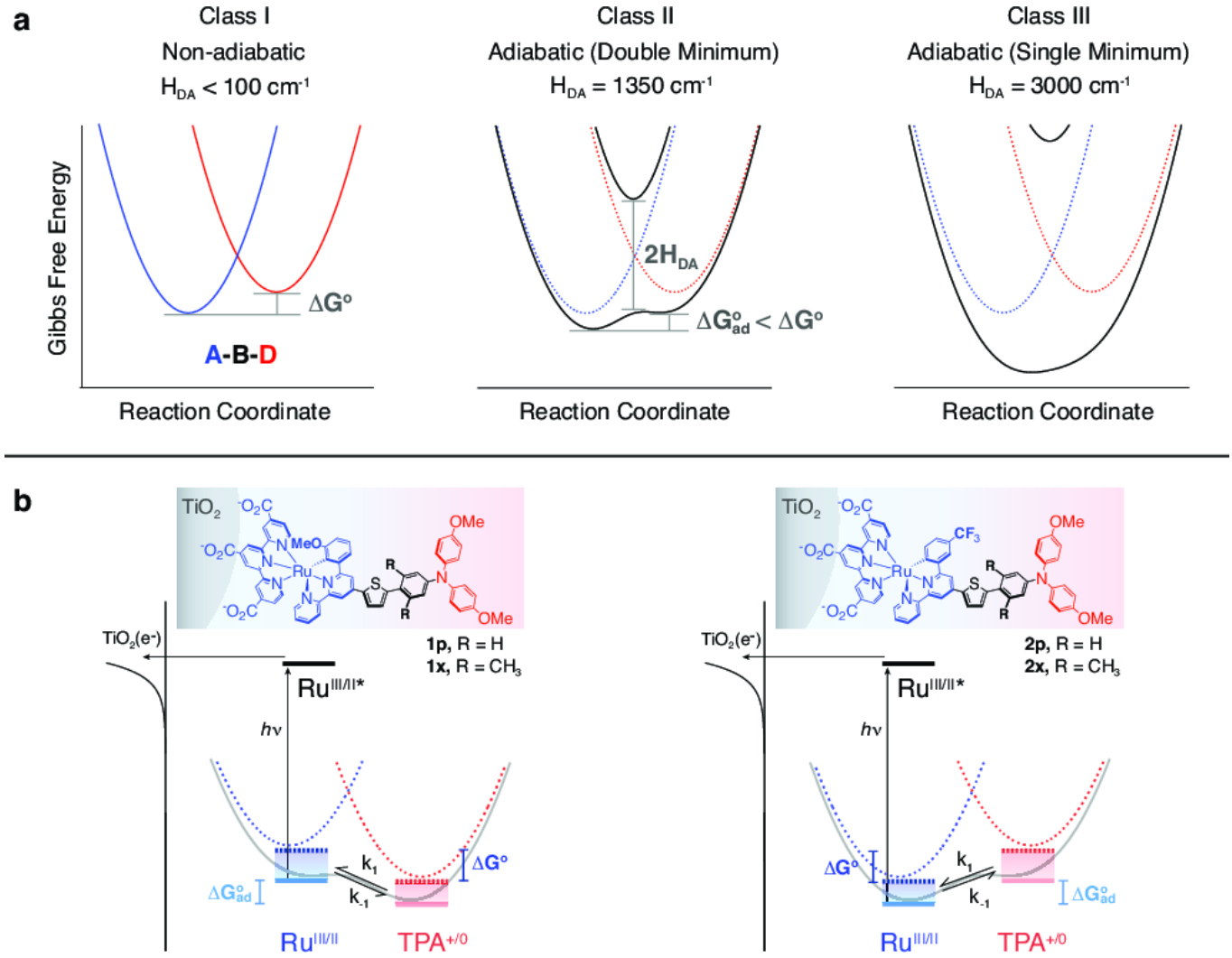

Fig. 2. The Gibbs energy surfaces and the kinetic approach. a, Gibbs free energy surfaces (GESs) that represent a redox equilibrium between A-B-D (blue) and A^--B-D^+ (red) as the electronic coupling matrix element (H_{DA}) is increased from 0 (nonadiabatic) to over 3000 cm^{-1} (adiabatic). Emphasis is placed herein on the reduction in the Gibbs free energy change, $|^{\triangle}G^{o}| > |^{\triangle}G^{o}_{ad}|$, that accompanies the transition from non-adiabatic to adiabatic electron transfer in the double minimum regime. **b,** The approach consists of a Ru^{II}-B-TPA compound anchored to the surface of mesoporous thin films of TiO_2 (the secondary acceptor). Light absorption induces excited-state electron injection from the Ru^{II} unit into the TiO_2 to form $TiO_2(e^-)$|-Ru^{III}-B-TPA. Within the time frame of charge recombination, the *dynamic* equilibrium Ru^{III}-B-TPA Ru^{II}-B-TPA^+ was quantified through a kinetic model that afforded the forward, k_1, and reverse, k_{-1}, electron transfer rate constants.

Table 1. Thermodynamic and Electronic Coupling Parameters at Room Temperature.

Compound	Electrochemistry[a,b]			Kinetics[a,c]	H_{DA} (cm^{-1})[d]
	$E^o(TPA^{+/0})$	$E^o(Ru^{III/II})$	$-^{\triangle}G^o/F$	$-^{\triangle}G^o/F$	
1x	940	860	-80 (0.044)	-80 (0.044)	< 100 (0.01)
1p	940	860	-80 (0.044)	-62 (0.089)	1350 (0.17)
2x	940	1010	+70 (16)	+68 (15)	< 100 (0.01)
2p	940	1030	+90 (35)	+54 (8.4)	1350 (0.17)

[a]Values given in mV vs. NHE. [b]Calculated with equation (2), using the electrochemical data, where *F* is the Faraday constant. Values in parenthesis are the equilibrium constants, K_{eq}. [c]Calculated with equation (2), using the kinetic data. Uncertainties in the values are ±10%. Values in parenthesis are the equilibrium constants, K_{eq}. [d]Values in parenthesis are given in eV.

where the TPA redox center was oxidized first, the more positive $E^o(Ru^{III/II})$ value likely emanates from the inductive influence of the oxidized TPA group transmitted through the strongly coupled *phenyl*-bridge. Nevertheless, $^{\triangle}E^o = E^o(Ru^{III/II}) - E^o(TPA^{+/0})$ was insensitive to the bridge identity for **1p** and **1x** and changed by 20 mV for **2p** and **2x**, Table 1.

Representative UV-vis absorption spectra of **2x** and **2p** anchored to an oxide surface, Fig. 3, show extinction coefficients for the *phenyl*-bridged **2p** compound that were about 30-50% larger than those measured for its *xylyl*-bridged analogue **2x**; consistent with greater electronic coupling afforded by the *phenyl* bridge.(16, 27) Density functional theory calculations (Fig. 3a-b insets) reveal

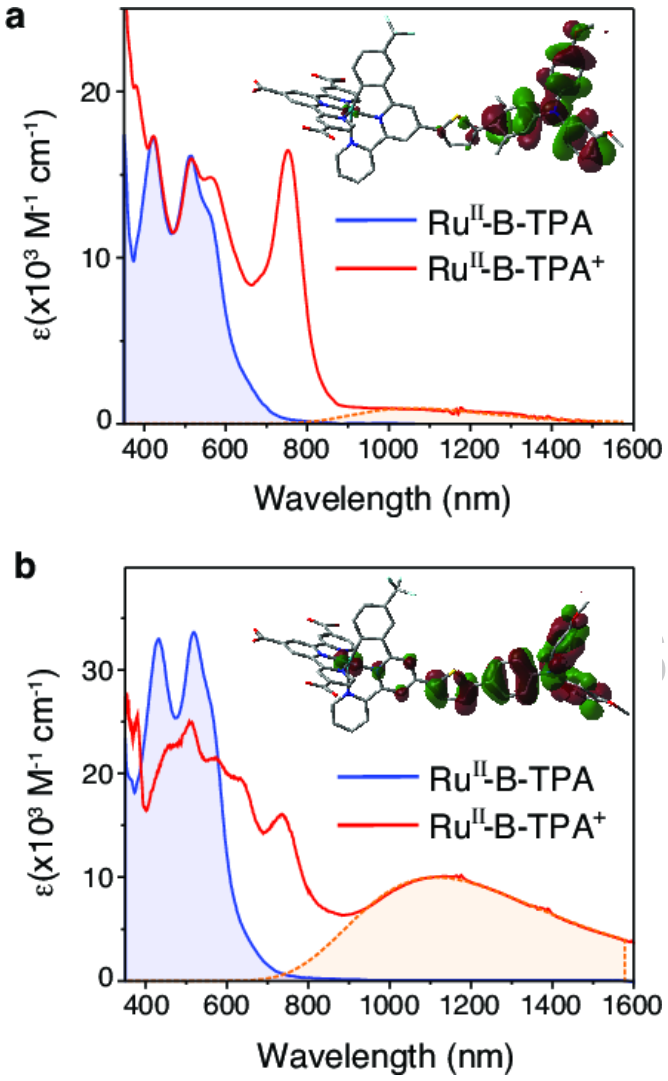

Fig. 3. Electronic properties. The visible absorption spectra of **2x** (**a**) and **2p** (**b**) anchored to In_2O_3:Sn thin films. Highlighted in the shaded orange area are the intervalence transition bands. The insets show the molecular structure with the overlaid highest occupied molecular orbitals (HOMO) generated from DFT calculations.

that the highest occupied molecular orbital (HOMO) for **2p** is more delocalized over the thiophene bridge and has both Ru and TPA character, while the HOMO for **2x** was localized predominantly on the TPA group. The appearance of an intervalence transition 'IT' absorption band centered around 1100 nm in the one-electron oxidized mixed-valent Ru^{II}-B-TPA^+ state enabled quantitative analysis of the electronic coupling. Application of the 2-state generalized Mulliken-Hush expression (28-30) provided: H_{DA} = 1350 cm^{-1} for **2p**; and H_{DA} < 100 cm^{-1} for **2x**. Electronic coupling values for (**1x**, **1p**) were estimated to be equivalent to those measured for (**2x**, **2p**), respectively, which indicated that the identity of the bridge unit, either *xylyl* or *phenyl*, determines the degree of electronic coupling.(31) The details of this analysis are given in the Supplementary Information.

Application of the kinetic approach

The transient spectra measured after pulsed green light excitation of **2x** and **2p** are given in Fig. 4a-b, respectively. The room temperature spectra reveal the appearance of an absorption band at ~ 750 nm that is characteristic of the oxidized donor TPA^+ that could be time resolved for **2x**, but not for **2p**. Hence the transient spectra alone provide direct evidence that the redox equilibrium is established more quickly for the adiabatic electron transfer reaction. In fact, the transient spectra recorded at any delay time after light excitation of **2p** were superposable when normalized, demonstrating that equilibrium was achieved on a sub-10 ns time scale at room temperature, whereas at lower temperatures, the appearance of TPA^+ could be partially time resolved (see below). The insets show kinetic data that corresponds to recombination of the injected electron with TPA^+ and the Ru^{III} center, the latter of which was much faster for the *xylyl* bridge.(16)

Temperature dependent kinetic data, over an 80 degree range, that report on the transient TPA^+ concentration for compounds **2x** and **2p,** Fig. 4c-d, are shown with overlaid kinetic fits. Under all conditions, the transient data fully recovered to initial values within 10 ms with no evidence of net photochemistry. The kinetic model utilized has previously been reported for excited-state acid base equilibria (24-26) and was constrained here with kinetic data from a model compound, that did not contain the pendant TPA group, which accounted for the non-exponential nature of the interfacial back electron transfer reaction (see Supplementary Information). The insets show the classical Arrhenius analysis of the k_1 and k_{-1} values extracted from the kinetic data. The observed temperature dependence, evident for all four compounds, is indicative of a significant activation barrier that provides clear evidence that the electronic coupling was insufficient to collapse the GES to a single minimum, i.e. Class III behavior, Fig. 2a.

For **1p** and **2p** (see Fig. S1b for **1p** data), the forward and reverse rate constants displayed the same temperature dependence. In sharp contrast, the introduction of the methyl substituents in **2x**, decreased the forward rate constant by over an order of magnitude, while k_{-1} also decreased significantly and became more temperature dependent. The expectation from transition state theory that the rate constant for the thermodynamically uphill reaction would increase with increasing H_{DA} was realized. The generality of this finding held true for the endothermic equilibrium of **1x** where kinetic analysis demonstrated that the uphill reaction, Ru^{III}-B-TPA → Ru^{II}-B-TPA^+, became more temperature dependent (see Supplementary Fig. 1a, inset). This is understood by an increased H_{DA} that lowers the barrier for the uphill reaction to a greater extent than for the exothermic reaction. For both *xylyl*-bridged compounds (**1x**, **2x**), the slow unfavored reaction rate constant approached the same value of that for the favored reaction as the temperature was raised. Classical Arrhenius analysis provided the barriers and pre-exponential factors for electron transfer, Table 2. The similar pre-exponential factors, ln(A), indicated that differences between adiabatic and non-adiabatic kinetics do not originate from changes in dynamic crossing events, but are instead controlled by a smaller activation barrier, E_a, for the uphill process, Ru^{III}-B-TPA → Ru^{II}-B-TPA^+ for **1p**, and Ru^{II}-B-TPA^+ → Ru^{III}-B-TPA for **2p**.

Classical van't Hoff representations(20) of the temperature dependent equilibrium data given in Fig. 5a and equation (3),

$$ln\ K_{eq} = -\frac{\Delta G^o}{RT} = -\frac{\Delta H^o}{RT} + \frac{\Delta S^o}{R} \qquad (3)$$

provide a vividly clear demonstration that K_{eq} was closer to unity for the *phenyl*-bridged (**1p**, **2p**) compounds, and hence $|\Delta G^o|$ was smaller for the more strongly coupled equilibrium. This finding is completely in line with theoretical predictions and the pioneering work of Kubiak and coworkers.(14, 15) Before discussing the broader impacts it is worthwhile to consider more carefully the specific data in Fig. 5a.

The van't Hoff plot demonstrates an adiabatic equilibrium for the *phenyl*-bridged compounds and a nonadiabatic one for the *xylyl*-bridged compounds. In other words, there is no evidence for thermal energy transfer at constant pressure for the *phenyl*-

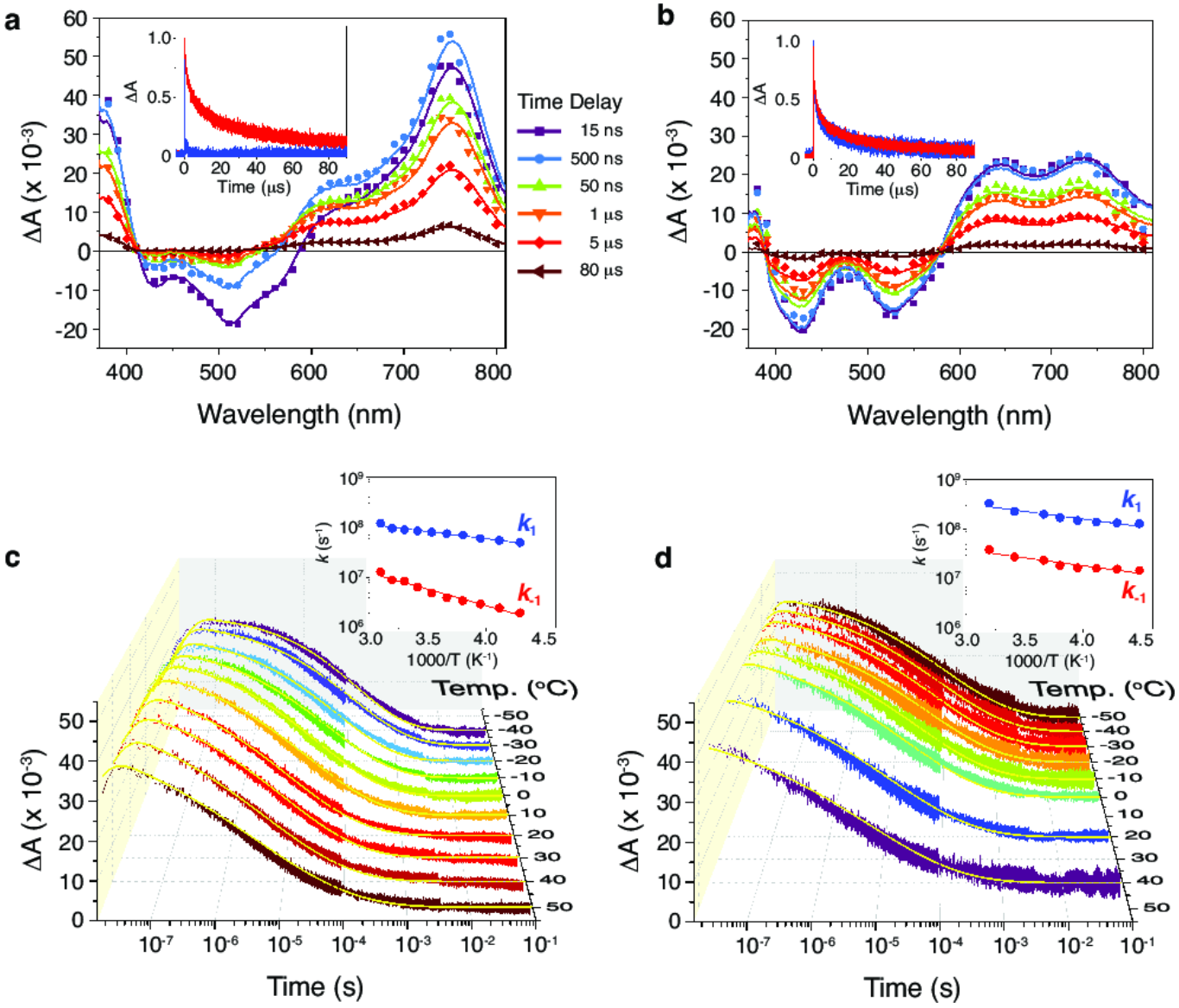

Fig. 4. Transient absorption data. (Upper) Absorption difference spectra measured at the indicated delay times after laser excitation for **2x** (**a**) and **2p** (**b**). The insets show normalized single wavelength kinetic data monitored at 700 nm (that reports predominantly on TPA^+ concentrations) and at 510 nm (due to Ru^{III}). (Bottom) Single wavelength data that reports on the time dependent TPA^+ concentration as a function of temperature for **2x** (**c**) and **2p** (**d**). Overlaid in yellow are fits to the kinetic model used, as described in the Supplementary Information. The insets display Arrhenius plots of the forward, k_1, and reverse, k_{-1}, rate constants. All experiments were performed in 0.1 M $LiClO_4/CH_3CN$ solution.

Table 2. Arrhenius Parameters Extracted from Temperature Dependent Rate Constants.

Compound	Ru^{III}-B-TPA → Ru^{II}-B-TPA^+		Ru^{II}-B-TPA^+ → Ru^{III}-B-TPA		Enthalpy[a]	Entropy[b]
	ln(A) k_1 (*uphill*)	E_a[a]	ln(A) k_{-1} (*downhill*)	E_a[a]	($\triangle H^o$)	($\triangle S^o$)
1x	22.0 ± 0.3	14.4 ± 0.6	21.8 ± 0.3	6.44 ± 0.6	7.9 ± 0.2	1.5 ± 0.8
1p	21.2 ± 0.2	4.8 ± 0.2	19.1 ± 0.1	5.40 ± 0.3	0.0 ± 0.3	-18 ± 0.6
	k_1 (*downhill*)		k_{-1} (*uphill*)			
2x	20.5 ± 0.2	5.4 ± 0.3	20.8 ± 0.3	12.5 ± 0.7	-7.0 ± 0.6	-2.6 ± 2.4
2p	21.7 ± 0.1	5.8 ± 0.7	19.6 ± 0.4	6.1 ± 0.8	0.0 ± 0.2	17 ± 2.4

[a]Values in kJ mol^{-1}. [b]Values in J mol^{-1} K^{-1}. Arrhenius equation, $k = A * exp(-E_a/RT)$.

bridged compounds, i.e. $q_p = \triangle H^o = 0$, Table 2. In contrast, the strong temperature dependence for **1x** and **2x** emanates from an enthalpically favored ($\triangle H^o$ = -7.0 kJ/mol) and unfavored ($\triangle H^o$ = +7.9 kJ/mol) electron transfer equilibrium, respectively. These data represent a notable contribution to the literature as calorimetric characterization of intramolecular electron transfer is difficult to obtain and most discussions of adiabatic *vs.* nonadi-

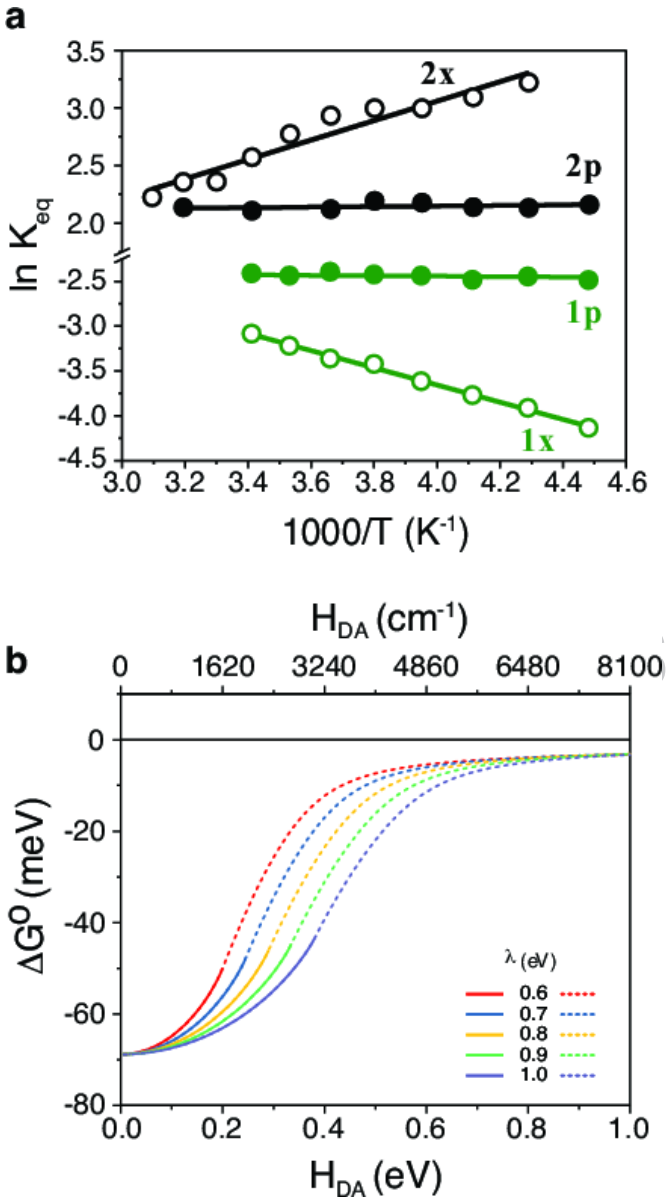

Fig. 5. van't Hoff analysis and the influence of electronic coupling on Gibbs free energy. a) A van't Hoff plot, ln K_{eq} vs 1000/T, of the electron transfer equilibrium constants with overlaid best fit lines that demonstrates an adiabatic mechanism for(**1p, 2p**) and nonadiabatic for (**1x, 2x**). **b)** Effect of electronic coupling on the Gibbs free energy for electron transfer calculated from numerical analysis of the GESs (equation (4)) with the indicated reorganization energies, λ. The solid lines represent the progression of the nonadiabatic $^{\triangle}G^{o}$ to the adiabatic value, $^{\triangle}G^{o}_{ad}$, limited to the double minimum regime. The dotted lines denote fictitious $^{\triangle}G^{o}_{ad}$ values for a GES collapsed to a single minimum.

abatic electron transfer are subjective, i.e. adiabaticity is inferred from rate constants or other observations.

Extrapolation of the *xylyl*-bridged data in the van't Hoff plot to higher temperatures suggests that a common equilibrium constant would be reached for the *xylyl*- and *phenyl*-bridged compounds around 350 K. At this temperature, thermal motion in the *xylyl* bridge is expected to provide sufficient coupling to access an adiabatic electron transfer pathway, however, the boiling point of CH_3CN precluded experimental confirmation of this. Notwithstanding the possibility of a slope change at higher temperature for *xylyl*-bridged compounds, the van't Hoff analysis indicated a small entropic contribution, $|\Delta S^{\circ}| = 2 \pm 3$ J mol^{-1} K^{-1}, whereas for the *phenyl*-bridged compounds $|\Delta S^{\circ}| = +17 \pm 3$ J mol^{-1} K^{-1} and provides the predominant contribution to ΔG^{o}. The enthalpies and entropies for the adiabatic and non-adiabatic reactions are presented in Table 2.

Free energy loss due to coupling

Significantly, the van't Hoff data reveal that $|^{\triangle}G^{o}|$ was smaller for the adiabatic equilibrium of both *phenyl*-bridged compounds over the entire 80 degree temperature range. This finding naturally raises two interrelated questions of relevance to maximizing the free energy stored in artificial photosynthesis: *1) How much free energy can be lost due to coupling?* and *2) What amount of coupling is necessary to collapse the double minimum GES into a single minimum?* The second question could be rephrased to ask, *when does H_{DA} become so large that the electron is delocalized over both redox centers such that equilibrium no longer has any physical meaning?* The answers to these questions depend on the magnitudes of $^{\triangle}G^{o}$, H_{DA} and the reorganization energy, λ.(12, 13) Fortunately, the ground- and excited-state GESs can be calculated exactly with equation (4) that has been previously reported (see also Supplementary Information).(12, 13)

$$G_{\pm} = \frac{[\lambda(2X^2-2X+1)+\triangle G^{o}]}{2} \pm \frac{[(\lambda(2X-1)-\triangle G^{o})^2+4H_{DA}^2]^{\frac{1}{2}}}{2} \quad (4)$$

The first derivative of the lower GES expression, G_{+}, provides x-intercepts that indicate the reaction coordinate X positions for the two minima and the transition state (provided that one exists) which can then be analyzed. An example is given below.

Consider **2x** and **2p** whose GESs, shown in Fig. 2, were generated from equation (4) with λ= 0.6 eV and $^{\triangle}G^{o}$ = -70 mV, H_{DA} = 0 eV for **2x**, and H_{DA} = 0.17 eV (1350 cm^{-1}) for **2p**. When H_{DA} is increased in the progression from 0 to 1 eV, the nonadiabatic $^{\triangle}G^{o}$ = -70 mV characteristic of **2x** remains essentially constant until about H_{DA} = 0.040 eV, Fig. 5. With increasing H_{DA} values, the adiabatic $^{\triangle}G^{o}_{ad}$ monotonically decreases and eventually the GES collapses to a single minimum, at the point where the solid lines become dashed in Fig. 5b, i.e. Class II → Class III behavior. At this point about 25% of the free energy is lost. Interestingly, the double minimum GES survives at much larger H_{DA} when λ is increased to 1.0 eV. Supplementary Fig. S3 and Fig. S4 shows that H_{DA} value necessary for collapse increases linearly with λ. We note that Dutton has shown that a λ of 0.6 eV for proteins and 1.0 eV for aqueous solution is sufficient to model much electron transfer data regardless of the medium that separates the A and D.(32-34) When $|^{\triangle}G^{o}|$ is greater than 70 mV, Class III behavior occurs at weaker electronic coupling. Indeed, for self-exchange reactions, when $^{\triangle}G^{o}$ = 0, the double minimum survives to H_{DA} = 0.5 eV for λ = 0.6 eV, Supplementary Fig. 4b. However, in self-exchange reactions, the products and reactants are the same and a free energy gradient for vectorial electron transport is lost. Nevertheless, concentration gradients have been successfully used to transport charge toward an electrode for solar cell applications.(35) In summary, this analysis indicates that the magnitude of $|^{\triangle}G^{o}|$ lost to electronic coupling is significant and should be considered in artificial photosynthesis design. As the open circuit photovoltage, V_{oc}, represents the maximum Gibbs free energy a regenerative solar cell can produce, the loss of > 10 mV is highly significant. Indeed, a 3 mV loss in V_{oc} was recently reported when a donor-acceptor adduct was formed and it is likely that this enhanced coupling turned on an adiabatic pathway.(36)

It is worthwhile to consider how natural photosynthesis utilizes electronic coupling to control the flow of electrons. In purple bacteria, H_{DA} is sufficient for adiabatic electron transfer in the special pair and the subsequent electron transfer steps are nonadiabatic.(2-4, 6) Other photosystems also show decreased electronic coupling when the redox active groups are more spatially separated from the excited-state.(2-6) Presumably these

photosystems evolved to efficiently transfer electrons when a kinetic competition with excited-state decay existed and the subsequent vectorial electron transfer steps occurred nonadiabatically to minimize free energy loss.(2-4, 6) The particular interfaces have been used in artificial photosynthesis, specifically in dye-sensitized solar cells.(16) It was found that the strong coupling afforded by the *phenyl* bridge resulted in more delocalized orbitals that promoted faster recombination of the injected electrons with the oxidized molecules.(16) It is now clear that a weakly coupled secondary donor should be employed with a small free energy gradient to translate the charge further from the interface. Therefore, natural and artificial photosynthesis utilize adiabatic pathways for electron transfer reactions that occur in kinetic competition with fast excited-state relaxation processes and nonadiabatic pathways to shuttle redox equivalents to catalytic or other redox active sites. The data reported herein indicates that the magnitude of the electronic coupling should be carefully tuned so as to minimize free energy loss.

The demonstration of a K_{eq} value closer to unity – or reduced $|{}^{\triangle}G^{o}|$ – values for electron transfer reactions that follow adiabatic, relative to nonadiabatic, pathways has broad implications. Taube indicated that adiabatic electron transfers were possible whenever $H_{DA} > 2kT$,(37, 38) and thus are potentially relevant to many classes of electron transfer in biology and chemistry including redox titrations that are commonly performed in undergraduate laboratories. Such bimolecular chemistry, and others in general, involves diffusion of the A and the D to form an encounter complex prior to electron transfer.(13, 39) The free energy change associated with the formation of the encounter complex is small in polar solvents and is usually neglected, but becomes more significant in low dielectric media.(40) If coupling within the encounter complex is strong at the instance of electron transfer, an adiabatic pathway may be operative that is expected to decrease the yield of products from that calculated based on formal reduction potentials. Indeed, a recent literature report of light driven bimolecular electron transfer in acetonitrile and ionic liquids with H_{DA} values between $\sim$100 – 1500 cm^{-1} showed that the rate constants could only be satisfactorily modeled when the ${}^{\triangle}G^{o}$ values were lower than those measured electrochemically.(4-1) This behavior is consistent with coupling lowering the free energy change. Indeed, when any encounter complex is sufficiently coupled, such as those that occur by an inner-sphere mechanism where an atom, ion or molecule, bridge the donor and acceptor, a loss in free energy should be anticipated.

Conclusions

In summary, light-initiated kinetic measurements have provided temperature dependent equilibrium constants for fundamental adiabatic *and* nonadiabatic electron transfer. It was found that the absolute value of ${}^{\triangle}G^{o}$ decreased for the adiabatic equilibria as was predicted theoretically decades ago.(12, 13). A virtue of adiabatic electron transfer is that equilibrium is rapidly achieved, but the data described herein show that this comes with a loss in free energy and more delocalized wavefunctions that can promote undesired reactions. Subtle structural changes were found to dramatically influence electron transfer reactions on the adiabatic/nonadiabatic borderline, and the results presented here teach how this influences fundamental chemical equilibrium. The data indicate that adiabatic pathways provide a more rapid approach to equilibrium that comes at the expense of some free energy loss.(19) On the other hand, the slower nonadiabatic path ultimately conserves more free energy in redox equilibrium and in vectorial transport chains for natural and artificial photosynthesis.

Experimental Section

All materials and reagents were used as received from the indicated commercial suppliers: acetonitrile (CH_3CN; Burdick & Jackson, spectrophotometric grade); Lithium perchlorate ($LiClO_4$; Sigma Aldrich, ≥ 99.99%); glass microscope slides (Fisher Scientific, 1 mm thick); fluorine-doped SnO_2-coated glass (FTO; Hartford Glass Co. Inc., 2.3 mm thick, 15 Ω/cm^2). All compounds were synthesized as previously described.(16)

Sample Preparation. Mesoporous thin films of TiO_2 nanocrystals and conductive tin doped indium oxide, In_2O_3:Sn, nanoparticles were prepared as described previously.(42, 43) The thin films were immersed in $\sim$ 1 x 10^{-4} M solution of the compounds and their absorbance values were monitored to obtain the desired surface coverage. Saturation coverages were necessary for electrochemical experiments with TiO_2 thin films while those on In_2O_3:Sn were performed at < 50% saturation coverages. To avoid intermolecular electron transfer reactions during transient absorption measurements, the absorbance of the thin films was controlled to assure < 50% surface coverage with TiO_2. Unless otherwise stated, all experiments were performed in 0.1 M $LiClO_4/CH_3CN$ solutions and samples were purged with argon gas for a minimum of 30 min prior to experiments.

UV-vis Absorption. The steady-state UV-visible absorption spectra were carried out with an Agilent Cary 5000 UV/Vis/NIR spectrophotometer at room temperature.

Transient Absorption. Nanosecond transient absorption experiments were performed on an apparatus as previously described.(16, 42) Variable temperature transient absorption data were obtained with a UniSoku CoolSpek (USP-203-B) liquid nitrogen cryostat. Kinetic measurements were taken after thermal equilibration at each temperature for at least 10 minutes.

Spectral modeling of the transient spectra obtained from kinetic analysis were performed using a least-square fitting (written in Mathematica 10) to the independently measured spectra of the singly oxidized Ru^{III} or TPA^{+} and the ground-state UV-vis spectra.

The variable temperature kinetic data were analyzed through a kinetic model described further below.

Electrochemistry. Spectroelectrochemical measurements were performed with an integrated UV-vis spectroelectrochemical system from Pine Research Instrumentation. Briefly, an Avalight Deuterium/Halogen (Avantes) was used as the light source and the AvaSpec ULS2048 UV-vis (Avantes) was the spectrophotometer. The WaveNow (Pine) operated as the potentiostat. The experimental setup consisted of a standard three-electrode cell with the sensitized thin films of TiO_2 or In_2O_3:Sn as the working electrodes, a Pt counter electrode (BAS), and a nonaqueous Ag/AgCl pseudoreference electrode (Pine). The ferrocenium/ferrocene ($Fc^{+/0}$) half-wave potential (+ 630 mV vs NHE)(44) was used to calibrate the pseudoreference electrode before and after experiments and to convert all measured potentials to the normal hydrogen electrode (NHE). Each applied potential was typically held for $\sim$2 min before UV-vis absorption spectrum was recorded. Fractional curves of each redox species were analyzed as a function of the applied potential. Integration of the Ru^{III} and TPA^{+} fractional curves yielded their respective Nernstian redox distributions. The formal reduction potentials, $E^{o}(Ru^{III/II})$ or $E^{o}(TPA^{+/0})$, were taken as the equilibrium potential where equal concentration of the two redox states were present. For NIR data, a BAS model CV-50W potentiostat was used in parallel with an Agilent Cary 6000i UV/Vis/NIR spectrophotometer at room temperature.

DFT Calculations. Ground-state geometries of **2p** and **2x** and their singly oxidized states were optimized using a fixed mixed basis set couple LANL2DZ (for the heavy metal Ru^{II}) and 6-31G(d) (for all other atoms), while the functional was varied between B3LYP and M06. Solvation effects were considered by using the C-PCM solvent model (CH_3CN, ε = 37.64). The effective charge transfer distance was calculated from the dipole moment change between the ground- and intervalence excited-state of the singly oxidized Ru^{II}-Bp-TPA^{+}, $r_{da} = {}^{\triangle}\mu_{eg}/e$ (see Supplementary Information for details). Calculations were carried using Gaussian 09 Package.(45)

Acknowledgements: The University of North Carolina (UNC) authors gratefully acknowledge support from the Division of Chemical Sciences, Office of Basic Energy Sciences, Office of Energy Research, U.S. Department of Energy (Grant DE-SC0013461). L. T.-G. would like to acknowledge the Belgian American Educational Foundation (BAEF) as well as the Bourse d'excellence Wallonie-Bruxelles International (WBI.World) for postdoctoral funding. The University of British Columbia authors are grateful to the Canadian Natural Science and Engineering Research Council (RGPIN 337345-13), Canadian Foundation for Innovation (229288), Canadian Institute for Advanced Research (BSE-BERL-162173), and Canada Research Chairs for financial support. The authors thank Victoria K. Davis for proof reading.

Supplementary Information. Experimental kinetic data for 1x and 1p, generalized Mulliken Hush analysis, kinetic modelling, derivation of Gibbs energy surfaces, and simulations of the electronic coupling influence on free energy. The Supplementary Information is available free of charge on the publisher website.

1. Winkler JR & Gray HB (2014) Electron Flow Through Metalloproteins. *Chem. Rev.*

114(7):3369-3380.
2. Cardona T, Sedoud A, Cox N, & Rutherford AW (2012) Charge Separation in Photosystem II: A Comparative and Evolutionary Overview. *Biochim. Biophys. Acta* 1817(1):26-43.
3. Romero E, Novoderezhkin VI, & van Grondelle R (2017) Quantum Design of Photosynthesis for Bio-Inspired Solar-Energy Conversion. *Nature* 543(7645):355-365.
4. Feher G, Allen JP, Okamura MY, & Rees DC (1989) Structure and Function of Bacterial Photosynthetic Reaction Centres. *Nature* 339(6220):111-116.
5. Whitmarsh J & Govindjee (2001) Photosystem II. *eLS*.
6. Barber J (1988) Electron-Transfer Theory in Question. *Nature* 333(6169):114-114.
7. Gust D, Moore TA, & Moore AL (2001) Mimicking Photosynthetic Solar Energy Transduction. *Acc. Chem. Res.* 34(1):40-48.
8. Gust D, Moore TA, & Moore AL (2009) Solar Fuels via Artificial Photosynthesis. *Acc. Chem. Res.* 42(12):1890-1898.
9. Wasielewski MR (1992) Photoinduced Electron Transfer in Supramolecular Systems for Artificial Photosynthesis. *Chem. Rev.* 92(3):435-461.
10. Kärkäs MD, Verho O, Johnston EV, & Åkermark B (2014) Artificial Photosynthesis: Molecular Systems for Catalytic Water Oxidation. *Chem. Rev.* 114(24):11863-12001.
11. Ashford DL, *et al.* (2015) Molecular Chromophore–Catalyst Assemblies for Solar Fuel Applications. *Chem. Rev.* 115:13006-13049.
12. Brunschwig BS & Sutin N (1999) Energy Surfaces, Reorganization Energies, and Coupling Elements in Electron Transfer. *Coord. Chem. Rev.* 187(1):233-254.
13. Sutin N (2007) Theory of Electron Transfer Reactions: Insights and Hindsights. *Progress in Inorganic Chemistry: An Appreciation of Henry Taube*, (John Wiley & Sons, Inc., Published Online), Vol 30, pp 441-498.
14. Ito T, *et al.* (2004) Observation and Dynamics of "Charge-Transfer Isomers". *Angew. Chem. Int. Ed.* 43(11):1376-1381.
15. Londergan CH, Salsman JC, Lear BJ, & Kubiak CP (2006) Observation and Dynamics of "Mixed-Valence Isomers" and a Thermodynamic Estimate of Electronic Coupling Parameters. *Chem. Phys.* 324(1):57-62.
16. Hu K, *et al.* (2016) Kinetic Pathway for Interfacial Electron Transfer From a Semiconductor to a Molecule. *Nat. Chem.* 8(9):853-859.
17. Marcus RA (1993) Electron Transfer Reactions in Chemistry. Theory and Experiment. *Rev. Mod. Phys.* 65(3):599-610.
18. Day P, Hush NS, & Clark RJH (2008) Mixed valence: origins and developments. *Phil. Trans. R. Soc. A* 366:5-14.
19. "Equilibrium" (2017) Equilibrium. in *Merriam-Webster.com* (Merrian-Webster).
20. Oxtoby DW, Gillis HP, & Butler LJ (2015) *Principles of Modern Chemistry* (Cengage Learning) 8th Ed.
21. Walker GC, Barbara PF, Doorn SK, Dong Y, & Hupp JT (1991) Ultrafast Measurements on Direct Photoinduced Electron Transfer in a Mixed-Valence Complex. *J. Phys. Chem.* 95(15):5712-5715.
22. Nelsen SF, Ismagilov RF, & Trieber DA (1997) Adiabatic Electron Transfer: Comparison of Modified Theory with Experiment. *Science* 278:846-849.
23. Lindeman SV, Rosokha SV, Sun D, & Kochi JK (2002) X-ray Structure Analysis and the Intervalent Electron Transfer in Organic Mixed-Valence Crystals with Bridged Aromatic Cation Radicals. *J. Am. Chem. Soc.* 124(5):843-855.
24. Laws WR & Brand L (1979) Analysis of Two-State Excited-State Reactions. The Fluorescence Decay of 2-Naphthol. *J. Phys. Chem.* 83(7):795-802.
25. Demas JN (1983) CHAPTER 4 - More Complex Systems. *Excited State Lifetime Measurements*, ed Demas JN (Academic Press), pp 43-69.
26. O'Donnell RM, *et al.* (2016) Photoacidic and Photobasic Behavior of Transition Metal Compounds with Carboxylic Acid Group(s). *J. Am. Chem. Soc.* 138(11):3891-3903.
27. Robson KCD, Koivisto BD, Gordon TJ, Baumgartner T, & Berlinguette CP (2010) Triphenylamine-Modified Ruthenium(II) Terpyridine Complexes: Enhancement of Light Absorption by Conjugated Bridging Motifs. *Inorg. Chem.* 49(12):5335-5337.
28. Cave RJ & Newton MD (1996) Generalization of the Mulliken-Hush Treatment for the Calculation of Electron Transfer Matrix Elements. *Chem. Phys. Lett.* 249(1):15-19.
29. Rust M, Lappe J, & Cave RJ (2002) Multistate Effects in Calculations of the Electronic Coupling Element for Electron Transfer Using the Generalized Mulliken−Hush Method. *J. Phys. Chem. A* 106(15):3930-3940.
30. Cave RJ, Edwards ST, Kouzelos JA, & Newton MD (2010) Reduced Electronic Spaces for Modeling Donor/Acceptor Interactions. *J. Phys. Chem. B* 114(45):14631-14641.
31. Piechota EJ, *et al.* (2018) Optical Intramolecular Electron Transfer in Opposite Directions Through the Same Bridge that Follows Different Pathways. *J. Am. Chem. Soc.* DOI: 10.1021/jacs.8b02715
32. Moser CC, Keske JM, Warncke K, Farid RS, & Dutton PL (1992) Nature of Biological Electron Transfer. *Nature* 355(6363):796-802.
33. Page CC, Moser CC, Chen X, & Dutton PL (1999) Natural Engineering principles of Electron Tunnelling in Biological Oxidation-Reduction. *Nature* 402(6757):47-52.
34. Osyczka A, Moser CC, Daldal F, & Dutton PL (2004) Reversible Redox Energy Coupling in Electron Transfer Chains. *Nature* 427(6975):607-612.
35. Moia D, *et al.* (2015) Dye Monolayers Used as the Hole Transporting Medium in Dye-Sensitized Solar Cells. *Adv. Mater.* 27(39):5889-5894.
36. O'Regan BC, *et al.* (2009) Structure/Function Relationships in Dyes for Solar Energy Conversion: A Two-Atom Change in Dye Structure and the Mechanism for Its Effect on Cell Voltage. *J. Am. Chem. Soc.* 131(10):3541-3548.
37. Sutton JE & Taube H (1981) Metal to Metal Interactions in Weakly Coupled Mixed-Valence Complexes Based on Ruthenium Ammines. *Inorg. Chem.* 20(10):3125-3134.
38. Reynolds WL & Lumry RW (1966) *Mechanisms of Electron Transfer* (The Ronald Press Co., New York).
39. Marcus RA & Sutin N (1985) Electron Transfers in Chemistry and Biology. *Biochim. Biophys. Acta* 811(3):265-322.
40. Troian-Gautier L, Beauvilliers EE, Swords WB, & Meyer GJ (2016) Redox Active Ion-Paired Excited States Undergo Dynamic Electron Transfer. *J. Am. Chem. Soc.* 138(51):16815-16826.
41. Wu B, Maroncelli M, & Castner EW (2017) Photoinduced Bimolecular Electron Transfer in Ionic Liquids. *J. Am. Chem. Soc.*
42. Argazzi R, Bignozzi CA, Heimer TA, Castellano FN, & Meyer GJ (1994) Enhanced Spectral Sensitivity from Ruthenium(II) Polypyridyl Based Photovoltaic Devices. *Inorg. Chem.* 33(25):5741-5749.
43. Farnum BH, *et al.* (2014) Photoinduced Interfacial Electron Transfer Within a Mesoporous Transparent Conducting Oxide Film. *J. Am. Chem. Soc.* 136(6):2208-2211.
44. Pavlishchuk V & Addison AW (2000) Conversion Constants for Redox Potentials Measured Versus Different Reference Electrodes in Acetonitrile Solutions at 25°C. *Inorg. Chim. Acta.* 298:97-102.
45. Frisch MJ, *et al.* (2010) *Gaussian 09, Revision B.01* (Gaussian, Inc., Wallingford CT).